# Improving Spectroscopic Performance of a Coplanar-Anode High-Pressure Xenon Gamma-Ray Spectrometer

Scott Douglas Kiff, Student Member, IEEE, Zhong He, Senior Member, IEEE, and Gary C. Tepper

Abstract—High-pressure xenon (HPXe) gas is a desirable radiation detection medium for homeland security applications because of its good inherent room-temperature energy resolution, potential for large, efficient devices, and stability over a broad temperature range. Past work in HPXe has produced large-diameter gridded ionization chambers with energy resolution at 662 keV between 3.5 and 4% FWHM. However, one major limitation of these detectors is resolution degradation due to Frisch grid microphonics. A coplanar-anode HPXe detector has been developed as an alternative to gridded chambers. An investigation of this detector's energy resolution is reported in this submission. A simulation package is used to investigate the contributions of important physical processes to the measured photopeak broadening. Experimental data is presented for pure Xe and Xe + 0.2  $\%\mathrm{H}_2$  mixtures, including an analysis of interaction location effects on the energy spectrum.

*Index Terms*—Coplanar anodes, gas detectors, high-pressure xenon, ionization chambers, position sensing, single-polarity charge sensing.

# I. INTRODUCTION

IGH-PRESSURE xenon (HPXe) ionization chambers are expected to be useful for border security applications due to their combination of detection efficiency, energy resolution, insensitivity to large temperature changes, and cost [1], [2]. One problem inhibiting these chambers is the potential for energy resolution degradation due to microphonic vibration of traditionally used Frisch grids. Many efforts have focused on replacing the Frisch grid with a functional equivalent, including rise-time compensation [3], [4], gridless geometries [5]–[7], and multiple-anode chambers [7]–[9]; one possible solution is the use of coplanar anodes, which is a subset of the final category.

The coplanar-anode HPXe detector discussed in this submission has been described in a previous publication [10]; a schematic is presented in Fig. 1, and Table I lists important parameters of this detector. The coplanar-anode HPXe chamber

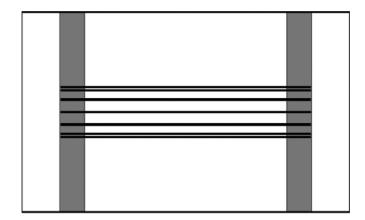
Manuscript received December 22, 2006; revised May 11, 2007. This work is supported under a National Science Foundation Graduate Research Fellowship and by the U.S. Department of Energy under NEER Grant DE-FG07-02ID14332 and NA-22 Award DE-FG07-06ID14727.

S. D. Kiff was with the University of Michigan, Ann Arbor, MI 48109 USA. He is now with Pacific Northwest National Laboratory, Richland, WA 99352 USA (e-mail: scott.kiff@pnl.gov).

Z. He is with the University of Michigan, Ann Arbor, MI 48109 USA (e-mail: hezhong@umich.edu).

G. C. Tepper is with Virginia Commonwealth University, Richmond, VA 23284 USA (e-mail: gtepper@vcu.edu).

Digital Object Identifier 10.1109/TNS.2007.903187



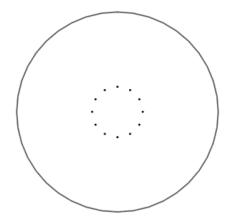


Fig. 1. Simplified cross-sectional schematics of the detector interior: anode wires are black, Macor structural material is dark gray, and white areas are filled with xenon. Top: Side view. Bottom: Cross-sectional view through the central active volume.

uses twelve 1-mm-diameter anode wires connected to form two independent anodes. These anodes are operated in coplanar mode to remove position sensitivity from the measured pulse amplitudes [11]. In addition, this detector is also capable of measuring the radial coordinate of gamma-ray interactions via the sum of the two anode signals, which is a function of the interaction radius; this capability has been documented in publication [12].

The coplanar-anode HPXe detector has achieved a measured energy resolution of 5.5% full-width at half-maximum (FWHM) at 662 keV using pure Xe. This performance is not competitive with other chambers of similar diameter, which usually attain 3.5%–4% or better [13]: one design has a reported energy resolution of 2.2%, the best published result to date for such a large chamber. Resolution degradation mechanisms are

TABLE I
A SUMMARY OF IMPORTANT DETECTOR PARAMETERS

Parameter	Design Value
Central detection volume length	101.6 mm
Cathode diameter	101.6 mm
Anode displacement from central axis	12.7 mm
Anode wire diameter	1.0 mm
Xenon density	0.3 g/cm <sup>3</sup>

investigated in this submission, and experimental improvements are implemented to improve the measured energy resolution. These experimental changes focus on doping the Xe gas with a  $\rm H_2$  cooling admixture to speed electron drift. Cooling admixtures have been in use since the first HPXe detectors were tested [14], and can improve the drift velocity at modest electric field intensities from about 1 mm/ $\mu$ s to over 3 mm/ $\mu$ s [15].

# II. SIMULATIONS

#### A. Simulation Methods

The detector simulations incorporate Monte Carlo methods with electrostatic simulations to create the best possible model of detector response. The Maxwell 3D electrostatic solver [16] has been used to simulate the operating electric field and weighting potential distributions within the detection volume. In these simulations, -4000 V is applied to the cathode, the collecting anode is held at +1400 V, and the noncollecting anode is grounded; these settings reflect typical experimental values.

The Maxwell 3D results have been used, along with electron drift velocity data [17], electron-ion recombination data [18] and electron cloud dimensions [10], to simulate preamplifier waveforms. These waveforms are shaped using a CR-RC<sup>4</sup> Gaussian filter. Geant4 [19] is used to simulate gamma-ray transport and interactions for an isotropically-emitting  $^{137}\mathrm{Cs}$  point source centered axially and located 25.4 cm from the outer surface of the pressure vessel. Electronic noise and Fano statistics, using the published mean energy loss per ionization ( $w=21.9~\mathrm{eV/ionization}$ ) and Fano factor (F=0.17) for compressed xenon gas [20], are also included in the Geant4 calculations. The final simulated energy and radius measurement [12] are tallied at this point to create energy spectra.

To implement these physical processes in the code, first the Maxwell 3D results are recorded on a Cartesian mesh (with the Z-axis parallel to the cylinder's axis) using spacing [0.2 mm, 0.2 mm, 8.0 mm] in the center region and [0.2 mm, 0.2 mm, 10.0 mm] in the end regions. Deposited energy is converted to a discrete number of charge carriers by application of w and F. The mean charge loss via recombination for a given gamma-ray interaction is determined using the data published in [18] and the electric field intensity at the nearest spatial node; stochastic treatment is considered by assuming Poisson statistics apply to the number of recombined electrons. If the size of the electron cloud is being considered, charge distribution is simplified by randomly distributing charge uniformly throughout a sphere of diameter 3.65 mm, the mean cloud diameter for full-energy depositions of 662 keV at this gas density [10]. Using 100-ns time steps, the electrons created in the interaction are transported using the local electric field intensity and direction, coupled with

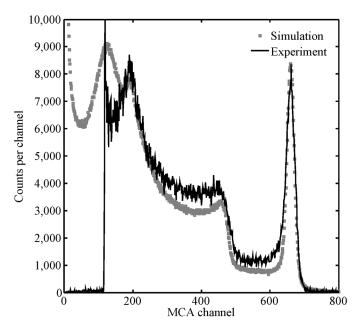


Fig. 2. A comparison of a measured  $^{137}\mathrm{Cs}$  energy spectrum to simulated data for similar system settings.

the electron drift velocity data of [17]. The weighting potential data is used at each time step to calculate the induced charge on the anodes using the Shockley–Ramo theorem [21]. The calculated anode signals are summed and subtracted for calculation of the position-independent pulse amplitude and the interaction radius, as described in [10] and [12]. Pulse filtering is applied to the anode sum and difference signals using Fourier transforms.

The simulation has been benchmarked against experimental data via a <sup>137</sup>Cs energy spectrum with similar system settings—see Fig. 2. It is clear that the photopeak shape is simulated correctly, although the experiment exhibits a low-energy tail that is not predicted by the simulations. It is possible that this is because x-ray escape is not considered in the modeling. Also, the Compton continuum shape is approximately correct, although lack of exact detail of the detector environment in the simulations probably accounts for the differences between the two spectra at energies below the photopeak. A lower-level discriminator terminates the experimental data at approximately 120 keV. The match between experiment and simulation is quite good in general, and it is reasonable to have confidence in the modeling for further studies.

This simulation package easily lends itself to quantifying the effect of each physical process upon the measured photopeak width. The desired results are obtained by creating tallies of the measured amplitude distributions after each physical process is added to the model. By creating several pulse-height spectra in this manner, it is possible to quantify the effect of each physical process by comparing the photopeak FWHM before and after each step of physics implementation; the FWHM of each process is assumed to sum in quadrature to obtain the overall FWHM. Starting from the true energy deposition spectrum, the quantified physical processes are as follows:

- 1) Fano charge carrier statistics;
- 2) weighting potential distribution;
- 3) charge recombination at the ionization site;

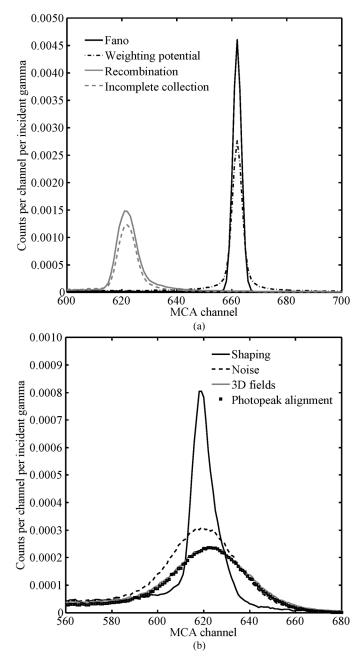


Fig. 3. Simulated measured response after each physical process has been added to the <sup>137</sup>Cs energy spectrum. Top: Photopeak distributions for processes unaffected by choice of shaping filter. Bottom: Peak distributions for processes dependent upon filter choice.

- 4) nonzero electron cloud radius;
- 5) nonideal charge collection due to insufficient biasing;
- 6) pulse shaping;
- 7) electronic noise;
- 8) axial electric and weighting field nonuniformities.

The first seven tallies assume the electric and weighting fields along the central detector plane are projected throughout the entire chamber; the final tally uses the true field distributions. The electric field exhibits nonuniform behavior along the axis due to peculiarities of the construction of this detector: for example, the cathode extends only between the Macor plates shown in Fig. 1, but the anodes reach nearly the full length of the chamber. This

TABLE II SIMULATED CONTRIBUTIONS OF EACH PHYSICAL PROCESS TO THE MEASURED PHOTOPEAK PROPERTIES

Process	FWHM (channels)	Centroid (channels)	Normalized peak area
True deposition	0	662	1.000
Fano statistics	3.74	662	0.993
Weighting pot.	2.28	662	0.785
Recombination	6.77	622	0.736
Cloud distribution	0.40	622	0.739
Improper V <sub>anode</sub>	(2.93i)	622	0.555
Shaping, geometry	6.52	620	0.556
Shaping, timing	2.70	619	0.520
Electronic noise	31.0	620	0.532
Axial nonuniform.	16.4	623	0.486
Peak alignment	(6.97i)	623	0.470

creates a weak field near the ends of the detector, but no field shaping rings have been employed to restore the field in the end regions.

The effects of pulse shaping can be split into two parts: a geometrical portion and a contribution due to timing. The geometrical factor considers the variation in shaped amplitude resulting from interactions in different sections of the detection volume, arising mainly from variations in the anode difference pulse shape. The timing factor acknowledges that due to the potentially long drift time of electrons in this system, a multiple-interaction event can suffer from pulse-height deficit. This deficit arises because the response of the shaping filter peaks at different times for each charge cloud created in the detector, and the time offset leads to a measured pulse amplitude less than the sum of responses when each cloud is considered individually.

The simulations are performed for a shaping time constant of  $12~\mu s$ , which provides the best experimental energy resolution. Photopeak FWHM calculations are performed by the peak fitting capabilities of EG&G ORTEC's MAESTRO-32 multichannel analyzer [22].

# B. Energy Resolution Contributions

The simulated energy spectra obtained after each process is considered are plotted in Fig. 3. Let us focus on the effects in the photopeak region, since this is the region of interest for energy resolution studies.

The effects of each process are quantified by assuming their contributions add in quadrature to obtain the final photopeak FWHM. These photopeak broadening contributions are listed in Table II, along with the effects on photopeak centroid and area. A graphical presentation of the FWHM contributions from each physical process can be found in Fig. 4. The two shaping filter effects are combined to present a total shaping filter contribution in Fig. 4, but are split into individual geometrical and timing contributions in Table II—refer to Section II-A for a discussion of these terms.

One point that will not be discussed further but is nonetheless important is that weighting potential, nonideal anode biases, and axial nonuniformity are all observed to remove a significant fraction of events from the photopeak. Weighting potential effects redistribute counts between 0 and twice the deposited energy, a peculiarity of coplanar anodes [23]. Nonideal

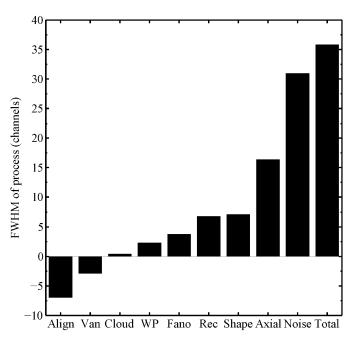


Fig. 4. Simulated contributions of each physical process to the overall  $^{137}\mathrm{Cs}$  photopeak FWHM; negative values indicate photopeak narrowing.  $V_{\mathrm{an}}$  represents nonideal electron collection due to improper anode biases.

anode biases and axial nonuniformity shift counts to lower channels due to imperfect electron collection and insufficient field strength, respectively. Imperfect electron collection occurs because without sufficient bias between the two anodes, it is possible for electrons to be collected on both sets of anodes. In coplanar anode theory all electrons are supposed to be collected by just one anode and the anode signal difference is then equal to the number of electrons collected in an interaction, but electron sharing between the anodes will lead to a post-differencing pulse height measurement that is less than the expected amplitude. Insufficient electric field strength in the end gas regions removes interactions from the photopeak via two effects: greater charge recombination and ballistic deficit, the latter caused by insufficient electron drift velocity.

The largest contributor by far to the measured photopeak width is electronic noise. After this process, the major contributors are axial field nonuniformity, the shaping filter, and charge recombination. The effect of charge recombination is not limited to an increase in the number of channels spanned by the photopeak FWHM, because recombination may substantially reduce the measured photopeak centroid via charge loss; both of these effects impact the measured energy resolution.

It is evident from this analysis that the axial field nonuniformity also is significant in determining the measured photopeak FWHM. Interestingly, a measured increase in the photopeak centroid accompanies this process. This effect is due to the strengthening of the fields near the central gas volume ends, an effect manifested via a reduced (yet broadened) charge recombination distribution (see Fig. 5, which plots the distribution of events after recombination for the central detector plane and for the plane z=48 mm, very near the edge of the central gas volume). This axial effect will be verified in collimation experiments presented in the following section.

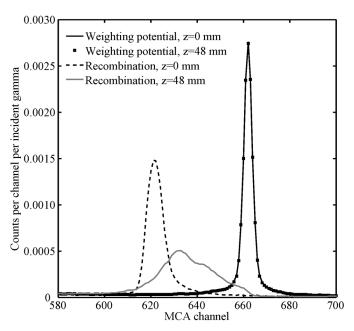


Fig. 5. Comparison of simulated recombination effects at the center plane and near the central gas volume's end (z = 48 mm).

From Table II, two processes are shown to have imaginary distribution widths, meaning they actually reduce the measured photopeak FWHM; they are presented graphically as negative FWHM values in Fig. 4. The first, improper anode biases, trades reduced photopeak area for improved energy resolution by removing counts from the photopeak that originate along field lines intersecting the noncollecting anode wires. These events would tend to lie near the upper end of the photopeak distribution, and removing them thus decreases the measured width. This effect has been observed experimentally by changing the interanode bias (see [10] for one example). The second process, photopeak alignment, uses the radial position-sensing capabilities of this chamber to compensate for the shift in photopeak centroid as a function of measured interaction radius, a process which effectively counteracts some of the degradation originating from weighting potential and charge recombination variations. Photopeak alignment is implemented by using the computed interaction radius to plot energy spectra as a function of calculated radius, as described in [12]. The photopeak centroid will drift as a function of radius due to changes in weighting potential and electric field intensity, but it is possible to correct for this centroid drift by applying a radially varying gain to align the photopeak centroids.

# C. Multiple-Site Events

For single-interaction events, generated via any physical process by which a gamma ray can deposit energy in the gas, the calculated radius is expected to be a good approximation to the actual interaction coordinate. Using theory developed in [12], the interaction radius  $r_0$  is related to the anode wire displacement from the central axis  $R_{\rm an}$ , the cathode radius

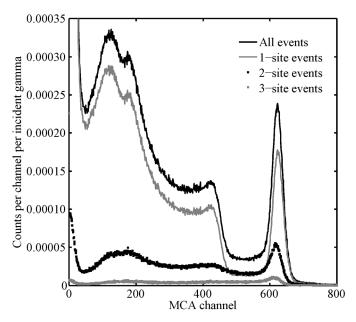


Fig. 6. All-event simulated  $^{137}{\rm Cs}$  energy spectrum plotted with the subsets including one, two, and three-site events.

 $R_{\rm cat}$ , and the anode weighting potential sum at the interaction location  $\varphi^{{
m sum},i}$  by

$$\frac{r_0}{R_{\text{cat}}} = \left(\frac{R_{\text{cat}}}{R_{\text{an}}}\right)^{-\varphi^{\text{sum},i}}.$$
 (1)

However, for multiple-site events, which are initiated by at least one Compton scatter inside the xenon gas and may be followed by a photoelectric absorption or pair production, the calculated radius is actually the product of the single-site radii for all N event sites weighted by drifting charge q created at each site, as follows:

$$\frac{r_0}{R_{\text{cat}}} = \prod_{n=1}^{N} \left(\frac{R_{\text{cat}}}{R_{\text{an}}}\right)^{-\frac{q_n \varphi_n^{\text{sum}, i}}{N}} \sum_{n=1}^{q_n} {q_n}$$
 (2)

Incident gamma rays that deposit energy in multiple locations are expected to degrade the energy spectrum because, generally, they cannot be compensated properly using the radial position-sensing information. To investigate this effect, the Geant4 simulation results previously described were grouped by the number of energy depositions in the fill gas. The results for a simulated <sup>137</sup>Cs energy spectrum prior to photopeak alignment are presented in Fig. 6; subsets with four and five or more events were recorded but are not presented due to the exceedingly-small frequency of such events. It is evident that most recorded events are from single-interaction sequences, and also that energy resolution appears to degrade as the number of interactions in a sequence increases.

The photopeak alignment procedure was applied to this simulated data, and again spectra were created from data subsets corresponding to single, double, and triple-site events. The measured energy resolution results (FWHM at 662 keV) are presented in Table III. Obviously, most of the improvement is due

Number of interactions	Resolution before peak alignment	Resolution after peak alignment
All	5.87%	5.76%
1	5.59%	5.43%
2	6.13%	6.02%
3	6.64%	6.89%

to the proper compensation of single-site events; interestingly, three-site events actually degrade after peak alignment is performed. This is related to the improper radius measurement: photopeak alignment attempts to compensate for variations in weighting potential and charge recombination as a function of radius, but since the measured radius for multiple-interaction events is generally incorrect, the applied compensation does not reflect the true conditions at each interaction site. Unfortunately, these predictions cannot be verified by experiments due to the inability to separate the collected data based upon the number of interactions per incident gamma ray.

#### III. EQUIPMENT PREPARATION AND EXPERIMENTS

## A. Hardware Description

The HPXe detector is described in detail in [10], and a schematic appears in Fig. 1; a summary of important parameters can be found in Table I. The detector utilizes a cylindrical geometry, with the cathode forming the outer boundary of the central gas volume and the anode wires located near the center of the detector. There are a total of twelve anode wires that are stretched axially through the detection volume, and they are arranged symmetrically about the main axis of the detector with uniform radial displacement and interwire spacing. The detector is filled with two gas mixtures: pure Xe and  $Xe + 0.2\%H_2$ . The latter gas mixture is used to increase electron drift velocity, as stated in the introduction. This is expected to improve the energy resolution either by allowing a reduction in shaping time from the parallel noise-dominated regime, or for a constant shaping time providing a reduction in ballistic deficit. Both noise and ballistic deficit are known to be important degradation mechanisms from the previous section's simulation results.

Although there are 12 wires, they are connected into two sets such that neighboring wires belong to opposing groups. Thus, there are two independent anode signals, and each anode is connected to an Amptek A250 charge-sensitive preamplifier. The two preamplifier outputs are directed to addition and subtraction circuits, which are used to obtain the deposited energy and the interaction radius (see [12]).

The sum and difference signals are filtered and amplified using analog shaping amplifiers, and the shaped signals are directed to a peak-hold circuit. The peak-hold circuit triggers when either channel rises above a threshold voltage, and the maxima of both signal amplitudes are held over a fixed measurement time span of about 48  $\mu s$  until finally the signal amplitudes are recorded and the circuit reset. These measured amplitudes are recorded by LabVIEW [24] from a National Instruments PCI-6110 data acquisition card. The amplitudes

are written to a data file for spectrum reconstruction at a later time.

#### B. Detector Preparation and Filling

For each experiment, the detector baking and filling was performed at a station previously described in [25], but with the xenon purified in a spark purifier. Xenon purification via the spark purification technique is described in [26], and is superior to gettering in terms of final overall gas purity. The detector and the filling station were baked at about 125 °C for several days to accelerate outgassing of the surfaces exposed to xenon, ensuring prolonged purity. The detector was filled to a density of 0.3 g/cm³, determined by the measured mass of xenon added and the known volume of the detector.

When  $H_2$  was used in experiments as a cooling admixture, it was passed through a room-temperature getter prior to filling, reducing the concentration of  $H_2O$ ,  $O_2$ , CO, and  $CO_2$  impurities to less than 1 ppb. The concentration of  $H_2$  in the fill gas was estimated with two techniques: first via the measured overpressure of  $H_2$  gas when the Xe was frozen with a liquid  $N_2$  bath, then with a mass spectrometer. Both measurements returned a  $H_2$  concentration near 0.2%.

# C. Equipment Settings

For all experiments, the collecting anode was biased to  $+1400~\rm V$  and the noncollecting anode held at ground; the cathode bias was set at  $-4500~\rm V$  for the pure Xe experiments and  $-4800~\rm V$  for Xe  $+0.2\%\rm H_2$ . The anode sum and difference signals were shaped with time constants of 16 and 12  $\mu\rm s$ , respectively. The former time constant was chosen to minimize ballistic deficit in the long-rising sum signal, the latter to optimize energy resolution. The gamma rays originated from a  $^{137}\rm Cs$  point source, in some instances collimated using lead bricks to irradiate 1/4-inch axial slices of the chamber. Each measurement lasted 30 min.

The radial interaction coordinate was estimated using the ratio of the anode sum and difference signals. The range of expected ratios was divided into 10 bins, appropriate for the expected uncertainty in the normalized coordinate of 0.055 to 0.077 [27]; extra bins were placed just outside this range to register unexpectedly high or negative radial coordinates. Energy spectra were grouped by measured radial bin to examine the effects of interaction location on the measured spectrum; the photopeak centroid was recorded as a function of radial position and a gain applied to each radial bin to align the photopeaks. This centroid drift is due to variations in both charge recombination along the  $\delta$ -ray tracks and weighting potential, and the peak alignment process compensates for these effects.

## D. The Effect of Cooling Admixtures

The measured rise times of the anode difference signal were generally around 2–3  $\mu s$  for photopeak events in the  ${\rm Xe}+0.2\%{\rm H}_2$  mixture, whereas the anode sum signal was always less than 20  $\mu s$  in rise time. These measurements indicate an increase in drift velocity by about a factor of two everywhere in the detector when compared to similar measurements with pure Xe fill gas.

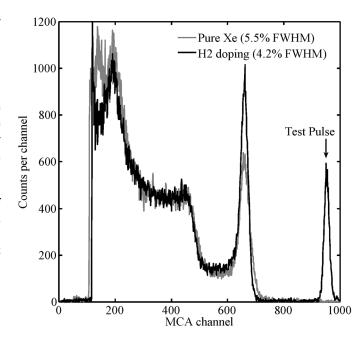


Fig. 7. Comparison of the pure Xe and the  $\rm Xe+0.2\%\,H_2$  collimated  $\rm ^{137}Cs$  spectra with photopeak alignment.

The effect of the cooling admixture can be observed in Fig. 7. For these experiments, the  $^{137}\mathrm{Cs}$  source was collimated upon the central axial plane of the detector. The change in gas mixture from pure to doped Xe improved the energy resolution from 5.5% to 4.2% FWHM; photopeak alignment is implemented in both of these measurements. The importance of photopeak alignment for this particular experiment is demonstrated by comparing the results before and after photopeak alignment for Xe + 0.2%H $_2$  gas, as done in Fig. 8: alignment improves the measured resolution from 5.7% to 4.2% FWHM.

# E. Collimation Effects

The placement of the collimated source beam is shown to have an effect on the measured photopeak FWHM and centroid—see the top panel of Fig. 9. Generally, as the source beam is moved toward the end of the central gas volume, the measured photopeak is observed to increase in both centroid location and FWHM: this outcome has been predicted and explained with simulations. The centroid shift is due to a reduction in charge recombination resulting from increased electric field magnitude near the end of the central gas volume. The photopeak broadening originates from the larger dispersion of field magnitudes near the central gas volume's end, increasing the variation in recombination. Although there is degraded performance near the end of the central gas region, the measured energy resolution is still improved compared to the best measurements with pure Xe.

The prominence of the Compton continuum is observed to increase with the likelihood of interactions near the ends of the chamber. This is expected, as the chamber ends have very weak fields that are known to contribute only to the continuum due to severe charge recombination and ballistic deficit. Experimental confirmation of this phenomenon is provided in the

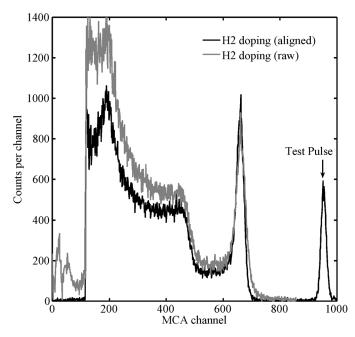


Fig. 8. Comparison of the  $\rm Xe+0.2\%\,H_2$  collimated  $^{137}\rm Cs$  energy spectra with and without photopeak alignment.

bottom panel of Fig. 9, where a centrally directed  $^{137}\mathrm{Cs}$  collimated beam and a beam irradiating one end region of the detector are compared under otherwise identical experimental conditions. The spectrum from the end region does not exhibit a photopeak, only a continuum extending to where the photopeak should reside.

# IV. CONCLUSION

From the simulations, it is apparent that the measured energy resolution is limited largely by electronic noise, followed by contributions from nonuniform axial fields, the shaping filter, and charge recombination. If one considers perfect electronics—i.e., zero noise—and further assumes that contributions from weighting potential, charge recombination, axial nonuniformity, and the geometrical shaping filter component can be perfectly compensated using position sensing information, then the measured energy resolution of these chambers should be around 0.7% based upon these simulation results. This set of conditions is certainly impossible to realize in practice, but points to the potential performance improvements if these effects can be minimized.

It is suggested that electronic noise be minimized by reducing the detector capacitance in conjunction with  $\rm H_2$  doping of the xenon gas, which can increase the electron drift velocity several times over for moderate electric field intensities [15]. This drift velocity increase will combine the improved parallel noise source contributions of shorter shaping times with the reduced ballistic deficit realized when the charge transit time is short compared to the shaping time constant. Other measures to reduce noise, such as preamplifier FET cooling, may also be beneficial.

An extension of position-sensing capabilities may help compensate for nonuniform detector response as a function of interaction location: one possibility is anode pixellation [9]. In ad-

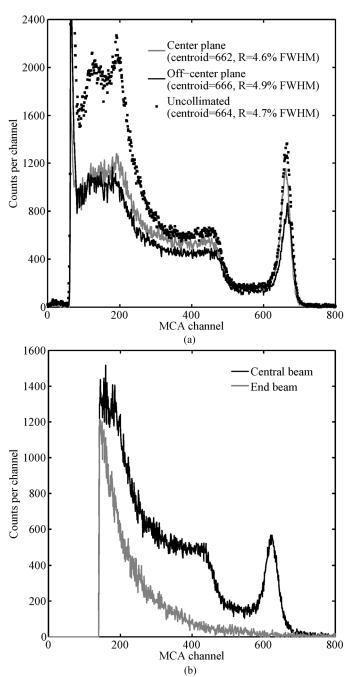


Fig. 9. Placement of the collimated beam affects the measured photopeak centroid and FWHM, as well as the peak-to-total count ratio. Top: Comparison of an uncollimated spectrum to beams collimated at the center and edge of the central gas volume. Bottom: Comparison of recorded spectra for a centrally collimated beam and a beam irradiating one end region of the detector.

dition, simulations suggest that multiple-site events broaden the photopeak while contributing only a small portion of the measured events. Extending the position sensitivity of the HPXe chamber may allow identification of multiple-site events, which can be either discarded or properly compensated using the local conditions at each deposition site.

The experiments proved the usefulness of cooling admixtures for improving the measured energy resolution of HPXe chambers. The addition of trace quantities of  $\rm H_2$  gas improved the measured energy resolution from 5.5% to 4.2% FWHM for a

collimated <sup>137</sup>Cs source. This new measurement is getting near the performance of similarly-sized gridded chambers, and in the future it is possible that improved coplanar-anode HPXe chamber designs will become even more competitive with their gridded counterparts.

The power of radial sensing is demonstrated via the photopeak alignment technique, which was shown to improve the measured energy resolution from 5.7% to 4.2% FWHM at 662 keV. This technique is easy to implement and compensates for the radial dependence of weighting potential and charge recombination. In theory, photopeak alignment can be made unnecessary by using extremely large electrode biases to reduce signal loss via charge recombination to the point at which it almost perfectly balances the charge induction deficits created by the weighting potential distribution, but position sensing makes the large biases unwarranted in practice.

Finally, the detector response was shown to vary as a function of axial position. To obtain the best performance possible, a new chamber design should be used in the future to minimize axial field variations within the central gas volume.

#### ACKNOWLEDGMENT

The authors would like to thank Dr. A. Bolotnikov of Brookhaven National Laboratory for many helpful discussions on cooling admixtures. The authors would also like to thank Dr. R. Kessick and Dr. P. Kiselev of Virginia Commonwealth University for their assistance in detector filling. Prof. L. J. Meng of the University of Illinois, Dr. D. Xu of GE Global Research, and Dr. B. Sturm of Lawrence Livermore National Laboratory have provided assistance with the Geant4 simulations.

### REFERENCES

- [1] V. V. Dmitrenko et al., "High-pressure xenon detector to identify and monitor nuclear materials," in 1996 IEEE Nuclear Science Symp. Conf. Rec., Anaheim, CA, 1996, vol. 2, pp. 938–941.
- [2] D. H. Beddingfield, A. Beyerle, P. A. Russo, K. Ianakiev, D. T. Vo, and V. Dmitrenko, "High-pressure xenon ion chambers for gamma-ray spectroscopy in nuclear safeguards," *Nucl. Instrum. Methods A*, vol. 505, no. 1–2, pp. 474–477, June 2003.
- [3] A. Bolotnikov and B. Ramsey, "Improving the energy resolution of high-pressure Xe cylindrical ionization chambers," *IEEE Trans. Nucl.* Sci., vol. 44, no. 3, pp. 1006–1010, Jun. 1997.
- [4] J. L. Lacy, A. Athanasiades, N. N. Shehad, L. Sun, T. D. Lyons, C. S. Martin, and L. Bu, "Cylindrical high pressure xenon spectrometer using scintillation light pulse correction," in 2004 IEEE Nucl. Sci. Symp. Conf. Rec., Rome, Italy, 2004, vol. 1, pp. 16–20.
- [5] V. V. Dmitrenko, A. S. Romanyuk, Z. M. Uteshev, and V. K. Chernyatin, "Spectrometric applications of an ionization-type drift chamber," *Instrum. Exp. Tech.*, vol. 25, no. 1, pp. 50–53, Jul. 1982.

- [6] R. Kessick and G. Tepper, "A hemispherical high-pressure xenon gamma radiation spectrometer," *Nucl. Instrum. Methods A*, vol. 490, no. 1–2, pp. 243–250, Sep. 2002.
- [7] A. E. Bolotnikov, R. Austin, A. Bolozdynya, and J. Richards, "Virtual Frisch-grid ionization chambers filled with high-pressure Xe," in *Proc.* SPIE 5540-Hard X-Ray Gamma-Ray Detector Physics VI, 2004, pp. 216–224.
- [8] C. J. Sullivan, Z. He, G. F. Knoll, G. Tepper, and D. K. Wehe, "A high pressure xenon gamma-ray spectrometer using a coplanar anode configuration," *Nucl. Instrum. Methods A*, vol. 505, no. 1–2, pp. 238–241, Jun. 2003.
- [9] Y. Feng, J. E. Baciak, C. Sullivan, and G. Gardner, "Pixelated designs of high pressure xenon gamma-ray spectrometers and position sensing," in *Proc. SPIE 6319-Hard X-Ray Gamma-Ray Detector Physics and Penetration Radiation Systems VIII*, 2006, p. 63191C.
- [10] S. D. Kiff, Z. He, and G. C. Tepper, "A new coplanar-grid high-pressure xenon gamma-ray spectrometer," *IEEE Trans. Nucl. Sci.*, vol. 52, no. 6, pp. 2932–2939, Dec. 2005.
- [11] P. N. Luke, "Single-polarity charge sensing in ionization detectors using coplanar electrodes," *Appl. Phys. Lett.*, vol. 65, no. 22, pp. 2884–2886, Nov. 1994.
- [12] S. D. Kiff, Z. He, and G. C. Tepper, "Radial position sensing in a coplanar-grid high-pressure xenon gamma-ray spectrometer," *IEEE Trans. Nucl. Sci.*, vol. 53, no. 3, pp. 1380–1384, Jun. 2006.
- [13] K. F. Vlasik, V. M. Grachev, V. V. Dmitrenko, S. E. Ulin, and Z. M. Uteshev, "High-pressure xenon  $\gamma$ -ray spectrometers," *Instrum. Exp. Tech.*, vol. 42, no. 5, pp. 685–693, 1999.
- [14] A. M. Galper, V. V. Dmitrenko, A. S. Romanyuk, and Z. M. Uteshev, "The possibility of creation of high sensitive gamma-telescopes based on pressed Xe for 0.1–10 MeV energy range," in *Proc. 17th Int. Cosmic Ray Conf.*, Paris, 1981, vol. 9, pp. 287–290.
- [15] V. V. Dmitrenko, A. S. Romanyuk, S. I. Suchkov, and Z. M. Uteshev, "Compressed-xenon ionization chamber for gamma spectrometry," *Instrum. Exp. Tech.*, vol. 29, no. 1, pp. 14–17, 1986.
- [16] Ansoft Corporation, Maxwell 3D ver. 9. Pittsburgh, PA, 2003.
- [17] J. L. Pack, R. E. Voshall, and A. V. Phelps, "Drift velocities of slow electrons in krypton, xenon, deuterium, carbon monoxide, carbon dioxide, water vapor, nitrous oxide, and ammonia," *Phys. Rev.*, vol. 127, no. 6, pp. 2084–2089, September 1962.
- [18] A. Bolotnikov and B. Ramsey, "The spectroscopic properties of high-pressure xenon," *Nucl. Instrum. Methods A*, vol. 396, no. 3, pp. 360–370, Sep. 1997.
- [19] CERN, Geant4 ver. 4.7. Geneva, Switzerland, 2005.
- [20] G. J. Mahler, B. Yu, G. C. Smith, W. R. Kane, and J. R. Lemley, "A portable gamma-ray spectrometer using compressed xenon," *IEEE Trans. Nucl. Sci.*, vol. 45, no. 3, pp. 1029–1033, Jun. 1998.
- [21] Z. He, "Review of the Shockley–Ramo theorem and its application in semiconductor gamma-ray detectors," *Nucl. Instrum. Methods A*, vol. 463, no. 1–2, pp. 250–267, May 2001.
- [22] EG&G ORTEC, MAESTRO for Windows ver. 5.10. Knoxville, TN, 2005.
- [23] Z. He, G. F. Knoll, D. K. Wehe, and J. Miyamoto, "Position-sensitive single carrier CdZnTe detectors," *Nucl. Instrum. Methods A*, vol. 388, no. 1–2, pp. 180–185, Mar. 1997.
- [24] National Instruments, LabVIEW ver. 8.0. Austin, TX, 2006.
- [25] G. Tepper and J. Losee, "High resolution room temperature ionization chamber xenon gamma radiation detector," *Nucl. Instrum. Methods A*, vol. 356, no. 2–3, pp. 339–346, March 1995.
- [26] A. Bolotnikov and B. Ramsey, "Purification techniques and purity and density measurements of high-pressure Xe," *Nucl. Instrum. Methods* A, vol. 383, no. 2–3, pp. 619–623, Dec. 1996.
- [27] S. D. Kiff, "Coplanar anode implementation in compressed Xenon ionization chambers," Ph.D. dissertation, Dept. Nucl. Eng. Radiol. Sci., Univ. of Michigan, Ann Arbor, MI, 2007, p. 107.